Technology Roadmap for Smart Iris Recognition

Zhenan Sun, Wenbo Dong, and Tieniu Tan
{znsun, wbdong, tnt}@ nlpr.ia.ac.cn
Center for Biometrics and Security Research &
National Laboratory of Pattern Recognition
Institute of Automation, Chinese Academy of Sciences
P.O. Box 2728, Beijing, 100190, P.R. China

Abstract

Iris recognition has many desirable properties for reliable individual authentication but usability is its largest bottleneck to wide deployment. Thus smart interface and machine intelligent are the objective of next-generation iris recognition. This paper presents the technology roadmap for smart iris recognition (SIR). Firstly, the concept of SIR is introduced, including its definition, characteristics and performance target. Then the evolution process of iris acquisition and recognition algorithm is proposed respectively. With various strategies of human-machine interaction, iris acquisition systems are grouped into seven categories, i.e. Close-range IR, Active IR, IR at a distance, Active IR at a distance, Passive IR on move, Active IR on move, IR for Surveillance. Iris recognition algorithms advance to be more accurate, robust, efficient and secure. The achievements of state-of-the-art iris recognition methods especially the contributions of our research group are reviewed in the roadmap.

Keywords: *Biometrics, Iris recognition, Technology roadmap.*

1. Introduction

Reliable individual authentication has important applications for both homeland and personal security. For example, accurate identification of criminals and terrorists leads to peaceful world. Secure verification of subjects to access bank accounts can avoid identity theft. With fast development of sensors, computers and algorithms, biometric traits such as fingerprint, face, iris, hand geometry, etc. are used for automatic personal identification [1]. Although fingerprint dominates the biometrics market now, it was predicted that iris recognition will become the most important biometric modality in the next 10 to 15 years [2]. Iris is the annular part of human eye between pupil and sclera (Fig. 1). There are mainly three desirable properties making iris recognition a particularly promising solution to security in the near future.

- Uniqueness: The uniqueness of iris pattern comes from the richness of texture details in iris images, such as freckles, coronas, stripes, furrows, etc. The randomly distributed and irregularly shaped microstructures of iris patterns make the human iris one of the most informative biometric traits. It is commonly believed that it is impossible to find two persons with identical iris patterns, even they are twins. The testing report of National Physical Laboratory of UK demonstrated that iris recognition is the most accurate biometrics [4].
- Stability: Iris texture is formed during gestation and stable across ages. So that the Afghan girl of National Geographic can be found even 17 years later based on her iris features [5].
- Non-invasiveness: Since the iris is an internal organ as well as externally visible, iris based personal identification systems can be non-invasive to their users, which is of great importance for practical applications.

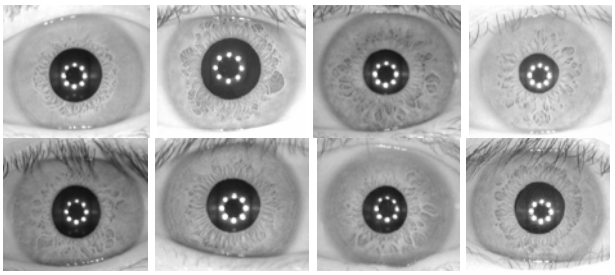

Figure 1: Some iris images from the CASIA database [3].

Flom and Safir first proposed the concept of automated iris recognition in 1987 [6]. Since then, research of iris acquisition and pattern recognition has achieved great progress. Recently, iris recognition has become an active topic in academia, industry and government. Iris recognition is playing a more and more important role in many mission-critical applications, such as assess control, national ID card, border crossing, welfare distribution, missing children identification, etc.

Our group has started research of iris recognition since 1998. We have experienced the fast development of iris recognition technology during the last ten years. However, “What is the future direction of iris recognition?” and “How to get there?” These questions are very important to researchers in iris recognition field but have never been addressed in literature, which motivates this paper to illustrate the technology roadmap of iris recognition.

Usability is the largest bottleneck of current iris recognition. So iris recognition is shift from “machine-centered” to “human-centered”, becoming easier to use with support of advanced hardware and software. Next-generation iris recognition must be smart and friendly to users. So we define the iris recognition systems in the future as SIR (smart iris recognition).

2. Overview of smart iris recognition

There are mainly three factors involved in the process of iris recognition: camera, algorithm and subject (Fig. 2).

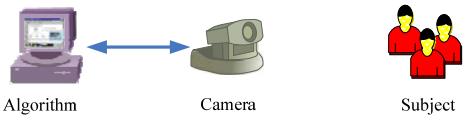

Figure 2: The diagram of iris recognition.

The variables of these three factors in iris recognition are summarized as follows:

- Camera: Active (Pan/Tilt/Zoom) or Passive camera; One camera or Multi-camera; Close-range or Long-range lens
- Algorithm: Variations in liveness detection/iris detection and tracking/ image quality assessment/image enhancement/iris localization/normalization/iris feature representation/iris feature extraction/iris feature

matching/iris database retrieval

- Subject: Single or Multiple subjects; Static or Move; Close to camera or At a distance

To make iris recognition accepted by subjects, the design principle of SIR must be human-centered rather than machine-centered. Then subjects never need to "stop, close, bend and stare" and they can enjoy the freedom of position and motion during iris recognition process. So the most compelling feature of SIR is that users are not required to intendedly cooperate with iris system. Iris images can be acquired and recognized unobtrusively and in real-time as a group of users are walking and at a distance to iris cameras. To support the friendly HCI (Human-Computer Interaction), iris acquisition system must be configured with multiple active cameras with long-range lens and iris recognition algorithms must be fast, robust, efficient and secure and adaptive to image quality. Here the main characteristics of SIR are listed as follows:

- Human-centered iris recognition
- Self-adaptive machine intelligence
- User-friendly HCI
- Cooperative multi-camera system
- Active detection, tracking and identification
- Iris recognition on the move
- Accurate identification result
- Robust recognition performance
- Efficient recognition process
- Fast matching engine
- Multi-user iris recognition at the same time
- High throughput
- Abnormal event report
- Self-protection

The performance targets of SIR are listed as follows:

- ✓ Number of users recognizable at the same time: 5 persons
- ✓ Head pose of users (Left/Right): $-90^{\circ} \sim 90^{\circ}$
- ✓ Head pose of users (Up/Down): $-30^{\circ} \sim 10^{\circ}$
- ✓ Standoff distance: 1~5 m
- ✓ Speed of movement: 2 m/s
- ✓ Recognizable zone (Height × Width × Depth): 1m × 3m × 2m
- ✓ Recognition time: <1 s
- ✓ False accept rate: <1/10,000,000
- ✓ Genuine accept rate: >99.9%
- ✓ Success rate of liveness detection: >99.99%
- ✓ Speed of iris matching: >100,000,000 records/second
- ✓ High throughput: 60 subjects/min
- ✓ Eyeglasses: Allowable

Iris recognition, as an interdiscipline, involves optics, electronics, mechanics, image processing, and pattern recognition. Advances of iris recognition are driven by both commercial applications and research problems. Both iris acquisition systems and iris recognition algorithms rapidly evolve in the last decade, with a common objective to make iris recognition easier. The following two sections describe the technology roadmap of iris acquisition and recognition algorithm respectively, including past, present and future. To better understand the evolution of iris recognition, it is necessary to review some representative works especially state-of-the-art.

3. Technology roadmap of iris acquisition

Iris image acquisition is an extremely important but hard problem. Iris images of low quality often result in false acceptance and false rejection and thus seriously affect the performance of a recognition system. However, iris acquisition is a very challenging problem due to the following reasons:

- The iris is fairly small (its diameter is about 1cm) but its resolution must be larger than 150 pixels in image. So DOF (depth of field) of iris acquisition system is limited.
- Many people especially Asians only exhibit abundant texture features under near infrared (NIR) lighting. So configuration of NIR lighting system is a big problem in iris acquisition.
- The iris should be optically on-axis and it is hard to detect and track iris due to its small size and head movement.
- When people wear eyeglasses it is challenging to capture qualified iris images due to specular reflections and dirty on eyeglasses.

With the enlargement of the biometrics market in the late 1990s, some corporations such as Sarnoff, Panasonic, LG, OKI etc. started to design iris image acquisition apparatus and develop iris recognition (IR) products based on efficient algorithms proposed in research community. With variation of the camera and user factors in iris recognition (Fig.2), we identify seven categories of iris acquisition systems in the history of iris recognition (Table 1). It is clear that iris acquisition is evolving from passive to active, close-range to long-range, static to dynamic, single camera to multi-camera (Fig. 3). So the position and motion constraints on users during iris recognition can be significantly reduced. Users will be pleased to use smart iris recognition in the future. But it should be noted that advanced technologies in iris acquisition need a time period to be mature for practical applications. The mainstream iris acquisition systems in current commercial market still belong to the simplest category, i.e. Close-range IR.

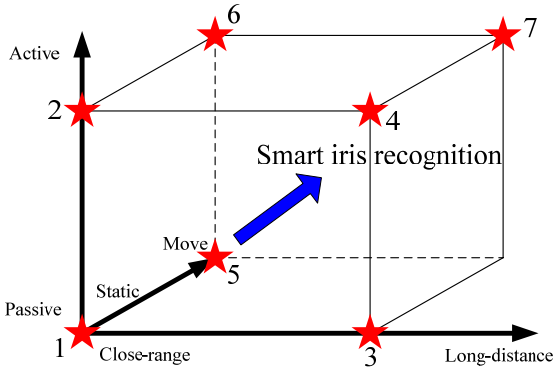

Figure 3: Technology roadmap of iris recognition.

3.1 Close-range IR

Close-range IR is based on fixed-focus lens and has limited DOF (around 10cm). Users need to stop and stare at the iris camera to get clear iris images in Close-range IR (Fig. 4). CASIA has done research for Close-range IR for ten years and developed a number of novel iris cameras (Fig. 5). Our experiences demonstrate that smart HCI is helpful to improve the ease-of-use of iris recognition. For example, the positioning system is designed to facilitate the user to precisely adjust the distance and focus angle between the user and the iris sensor for non-invasive imaging. It may include the distance measurement sensors and external indicator lights, mirrors and screen for feedback. The physical capture system consists of a central control unit, a family of optical lens, frame grabbers and CCD or CMOS cameras, and so on. The central control unit coordinates other units by analyzing the successively collected information and sending out reasonable instructions. Besides hardware design, software modules such as eye detection, image quality assessment, eyeglasses detection and liveness detection

can help the central control unit make decisions in iris acquisition.

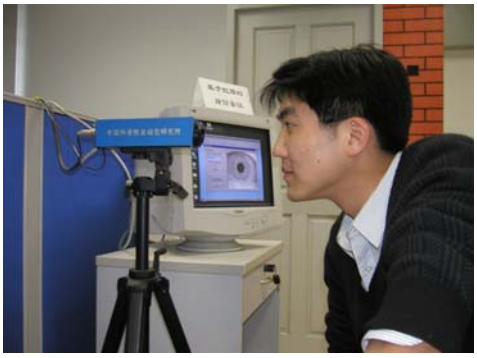

Figure 4: Example of close-range iris recognition.

Figure 5: Close-range IR cameras developed by CASIA.

Iris image acquisition is a non-trivial issue and one of the main difficulties is how to set the near infrared illuminators so that an iris pattern is uniformly illuminated and the highlight spots due to NIR illuminators' specular reflections are well controlled in the pupil region. Almost all commercial iris cameras' illumination system generates only one major spot in the iris image which is often far from the pupil center. This configuration leads to non-uniform illumination in the iris region. Experiences show that clear iris texture details cannot be captured without strong and uniform infrared illumination. We have designed a circular NIR LED array, with suitable luminous flux for iris imaging, which has successfully solved the illumination problem in iris imaging. Our iris camera can capture very clear iris images whose quality is often much better than others (see Fig.1). The arrangement of the NIR LED array (and hence our novel design of NIR illumination) can be clearly seen in the specular highlights in the raw iris images as shown in Fig.1.

We have constructed CASIA Iris Image Database [3] using self-developed iris cameras and released it to the public domain since 2002. The users of CASIA database have been increased to 2,400 research groups of 70 countries or regions. The CASIA Iris Image Database is gradually enlarged to include more images taken by various sensors from more races. Now CASIA-IrisV3 includes three subsets, containing a total of 22,051 iris images from more than 700 subjects. It is probably the largest iris image database in size in the public domain.

3.2 Active IR

Close-range IR statically waits for subject entering capture volume, i.e. camera-centered rather than human-centered. In contrast, active iris acquisition system is self-adaptive to the position and motion of subjects. This involves two problems: one is "how to find iris?" and the other is "how to align the camera with iris?" Compared with small iris, face is easier to be detected in cluttered background. So it is a common practice that a wide-angle camera for face capture is added into iris acquisition system [9][11][12]. Once face is detected in wide-angle view, then the position of dual-eye is estimated based on pre-calibrated coordinate system between face and iris cameras. Finally, the iris camera is controlled by a pan-tilt-unit (PTU) moving towards the iris region. If iris is on the depth-of-field, the auto-focus iris camera can capture clear iris images.

Figure 6 shows the prototype of active IR camera developed by CASIA [12]. Our system is based on low-resolution face and iris cameras, with low-price and high frame rate (30 fps). Face and iris cameras, along with the NIR arrays are co-located in PTU. Our active iris acquisition system is simple and compact but performs well. It can capture high-quality iris image in the range of 0.6m×0.4m×0.4m in average 3 to 5 seconds.

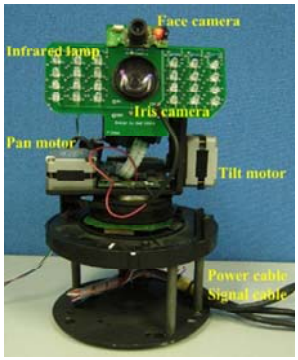

Figure 6: Active IR camera developed by CASIA.

3.3 IR at a distance

Fancourt et al. verified the possibility of capturing qualified iris images at a distance (5m, 10m) [10]. They developed a complex optical system based on telescope and infrared camera. The shortage of this system is that users need to fix their head to a position. So such an iris acquisition system has no potential for commercial applications, but it is a necessary stage in iris recognition roadmap. The experiences accumulated in this project are helpful for Sarnoff to develop Iris Recognition on the Move [13].

3.4 Active IR at a distance

A straightforward improvement of the user interface of IR at a distance is to use the active imaging techniques presented in Section 3.2. We have recently developed an active iris acquisition system for long-range iris recognition (Fig.7), which has three novelties compared with the IR at a distance [9].

Figure 7: Active IR at a distance developed by CASIA.

Firstly we use a high-resolution camera (2352×1728 pixels) with fast speed (15 fps) and an 300 mm focus lens to build an iris acquisition system at 3 meters of standoff distance, which can capture clear iris images (Fig. 8) in a volume of about 16cm×12cm×10cm in real time. The diameter of iris is around 180 pixels in captured iris images, which is much better than the 128 pixels in IR at a distance [10] and the 100 pixels in IR on

the move [13].

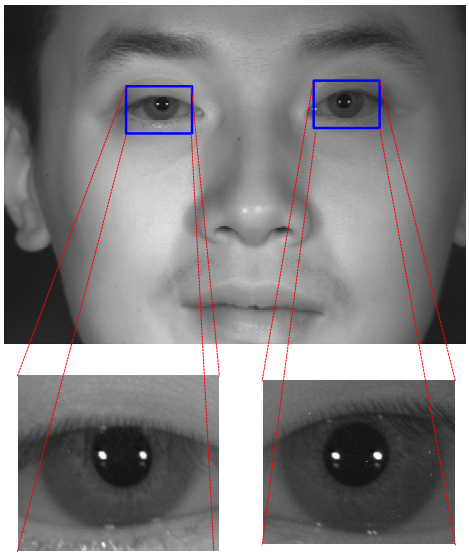

Figure 8: Example iris images captured by Active IR at a distance.

Secondly, a pan-unit is used to automatically adapt to different heights of people based on the face location in wide-angle view.

Thirdly, a LCD screen and sound indicator are used to guide users into the capture volume. People can see their face and eyes images in the front screen and adjust themselves to the right position.

Our active IR at a distance has been tested by more than 200 users. Experiments show that the whole procedure of image acquisition, processing and iris recognition only takes about 3 seconds with extremely high accuracy. Even people wearing eyeglasses can be correctly recognized by our system.

3.5 Passive IR on move

Matey et al. in Sarnoff Corporation proposed the concept of "Iris on the Move" (IOM) [13] and developed a prototype for potential use in commercial applications. The basic idea of IOM is to capture iris images when subjects walk through an access control point at normal walking speed (<1m/s) without pause [13]. Multiple high-resolution iris cameras are mounted on the portal, covering a capture volume 20cm×40cm×10cm. It is estimated at lease one in-focus image can be captured as the subject walks through the system [13]. High-power LED arrays are flashed to provide strong NIR illumination for iris imaging by video synchronization.

However, the recognition rate of the IOM is not very good due to poor quality (blur, low-resolution) iris images and specular reflections in iris texture. But the idea of "Iris Recognition on the Move" is promising and represents the future direction of iris recognition.

3.6 Active IR on move

IOM [13] indeed adopts passive iris acquisition scheme, using iris cameras of fixed lens, without support of Pan-Tilt units. So IOM can only wait for the presentation of iris when subject passing through the narrow depth of field (10 cm). A possible way to extend the capture volume of IOM is to be more active in iris acquisition. Because subjects are determined to walk towards access control point, it is easy to track the movement of human eyes in defined trajectory. With a high-speed auto-focus iris camera or a camera array with variable focal lengths, we can have more than one chance to capture the clear iris images. So active acquisition of moving subjects at a distance is promising to become a reality in next a few years.

3.7 IR for Surveillance

The above iris acquisition systems are mainly proposed for positive personal identification. When legitimate users request assess to computer, building, homeland, etc. they fully cooperate with iris recognition systems to make them identified. In contrast, when police like to check the identity of each subject at crowded subway against a database of the most wanted criminals and terrorists, covert iris image capture and negative personal identification is required. In such a security surveillance application, you can not require everybody to line up and go through a portal one by one. Thus efficient iris acquisition of a group of subjects without any constraints on pose, position and movement in cluttered background is a grand challenge.

IR for surveillance of wide areas requires a network of iris cameras, being active, intelligent and collaborative in iris acquisition. In covert iris recognition, the image quality can not be guaranteed. Facial features, height information and other soft-biometrics may be combined with iris textures to finally determine the identity of an individual. Covert iris recognition is a part of a video surveillance system, rather than an independent module. Although IR for surveillance is a number of years away, it has very important applications in homeland security and is of great interest to government agencies [14]. For example, the Defense Advanced Research Projects Agency (DARPA) of US has started the HumanID (Human Identification at a Distance) program since 2000, with the objective to develop automated biometric identification technologies such as face, iris, gait etc. to detect, recognize and identify humans at great distances.

4. Technology roadmap of iris recognition algorithms

Iris recognition algorithm transforms input iris image into identity after a number of steps: image quality assessment, liveness detection, iris localization, normalization, feature extraction, feature matching and database retrieval.

Daugman proposed the first successful algorithm for iris recognition [15]. In this algorithm, integrodifferential operator is used to localize the circular boundaries of iris region. Then iris texture is normalized to polar coordinate system using linear mapping. In feature extraction, even and odd Gabor filters are proposed to demodulate phase information in each iris region. And phase value is coarsely quantized to 2-bit binary codes so that a given iris image is represented with 256 Bytes iris code. At the feature matching step, the dissimilarity between two iris codes was measured by Hamming distance. Daugman's algorithm has been widely used in commercial iris recognition products.

Great progress has been achieved on iris recognition method since last decade. Testing results of both International Biometrics Group (FRR=2~5% @ FAR=10^{-6}) [16] and Iris Challenge Evaluation in 2006 (FRR=1~3% @ FAR=10^{-3}) [17] demonstrate that the state-of-the-art iris recognition algorithms perform well on most of qualified iris images. So the future efforts should pay more attention to processing and recognition of poor quality iris images. Iris recognition algorithm should be more accurate, robust, efficient and secure. This trend is demonstrated as follows with some examples.

4.1 Iris localization

Most of iris localization methods in literature are based on the assumption that the boundary of iris is circular, but a small part of iris images have irregular shape of pupil and limbic boundaries. So we propose multi-arc model to fit the noncircular boundary of iris pattern and achieve improved recognition performance (see Fig. 9). Daugman's new method models inner and outer boundaries of iris with active contour [18]. Other challenging problems in iris localization include off-axis iris images, occlusion of eyelids and eyelashes, specular reflections

due to eyeglasses, etc. With proposal of new and image adaptive algorithms, the last 1% challenging iris images are promising to be precisely localized. At last, sophisticated iris region segmentation method can perform comparable to Human Visual System.

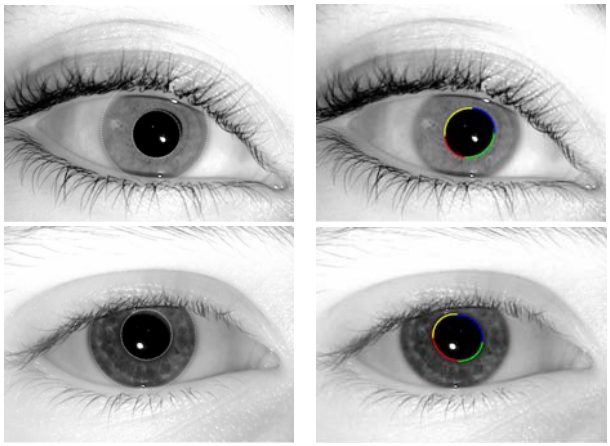

Figure 9: Iris localization based on multi-arc fitting method. The left column shows iris images localized using circle model and the pupil of iris images in the right column are fitted with four arcs. The two example iris images are from ICE [17].

4.2 Iris normalization

Pupil dilation and contraction caused by illumination changes result in the nonlinear deformation of iris texture (Fig. 10). For example, pupil diameter may range from a minimum of about 1.5mm to a maximum of over 7mm. Such a distortion of iris texture enlarges intra-class variations and increases the False Reject Rate (FRR). So iris normalization is important to iris recognition as it intends to reduce the effect of iris deformation. As the majority of iris recognition systems employ linear normalization method based on rubber sheet model, spatial misalignment of iris features has become the main cause of false rejection errors. We propose an efficient method to correct nonlinear deformation of iris texture [19]. Gaussian function is used to approximate the additive deviation of nonlinear iris stretch [19]. Our method achieved significant improvement over linear normalization model, making iris recognition more robust in realistic environments [19]. Since the mechanism of pupil dilation and contraction is still unknown, more precise non-linear iris normalization model is promising to be proposed in the future.

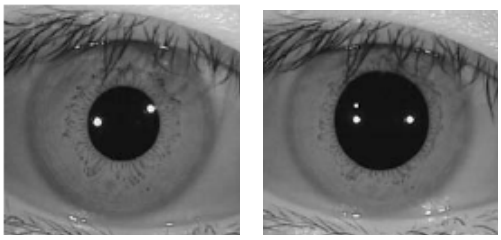

Figure 10: Example of iris deformation caused by pupil dilation. These two iris images are from the same eye but differ in pupil diameter.

4.3 Iris liveness detection

The success of spoofing iris recognition systems with fake iris pattern raises the security problem of iris recognition [20]. Fraudulent iris images may be printed on paper and contact lens, displayed in video, shown by glass eyes (Fig.11). The countermeasures proposed by Daugman include motion of pupil, high-frequency energy, etc. [21]. However, pupil hippus is also observable when people wear contact lens and the high-frequency features are not stable when iris images are noisy or blurred. Our solution to iris liveness detection is statistical texture classification [22]. Three anti-spoofing measures are proposed to detect color contact lens in iris recognition, i.e. iris edge sharpness, statistical distribution of iris-textons, selected textural features based on co-occurrence matrix [22]. The correct classification rate on a dataset including 640 fake iris images is more than 95%. Although our iris liveness detection algorithm achieved state-of-the-art performance, there is still much room to be improved.

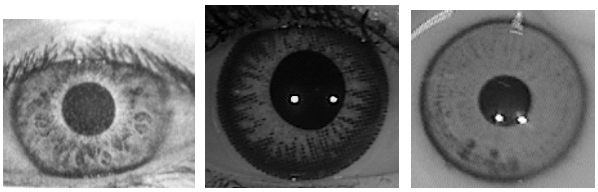

(a) (b) (c)

Figure 11: Fake iris images. (a) Iris printed on paper. (b) Iris printed on contact lens. (c) Iris pattern of glass eye.

4.4 Iris feature representation

A key and still open issue in iris recognition is how to effectively represent such textural information using a compact set of features (iris features). There is no commonly acknowledged standard of iris features. We propose to use ordinal measures for iris feature representation with the objective to characterize qualitative relationships between iris regions rather than precise measurements of iris image structures (Fig.12). Such a representation may lose some image-specific information but it achieves a good trade-off between robustness and distinctiveness. We show that ordinal measures are intrinsic features of iris patterns and largely invariant to illumination changes. Moreover, compactness and low computational complexity of ordinal measures enable highly efficient iris recognition.

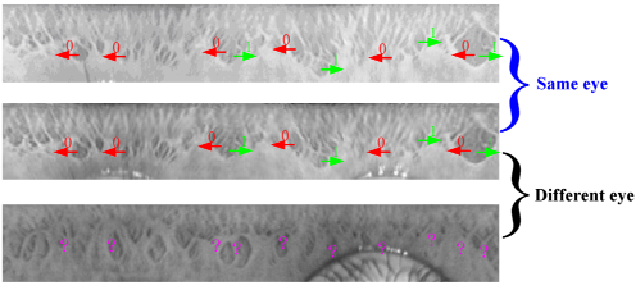

Figure 12: Comparison of intra-class and inter-class ordinal measures in normalized iris images. The upper two iris images are from the same eye, and their ordinal measures are largely invariant even under different illuminations. However, the probability of matching ordinal measures of inter-class iris images is only around 50%.

With flexible intra-lobe and inter-lobe parameters such as location, scale, orientation and distance in image filtering (Fig.13), ordinal measures (OM) form a general framework for iris feature representation and extraction. Specific iris coding schemes can be obtained under the guidance of this framework by changing parameter configurations of ordinal filter. Furthermore, with the OM representation model in place, we demonstrate that iris image features of a number of best-performing iris recognition methods may be interpreted as special cases of this model.

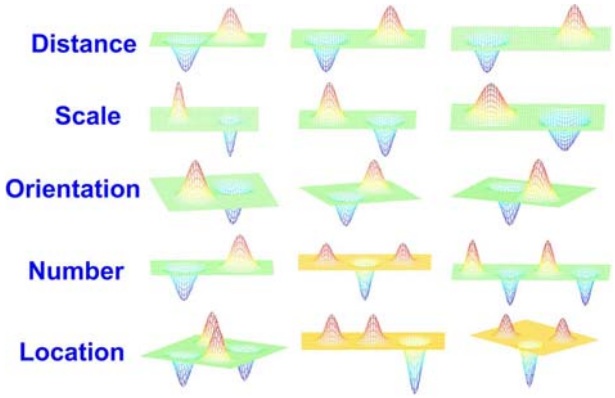

Figure 13: Variable ordinal measures.

Since ordinal measures are determined to be very suitable to describe iris features, the roadmap of iris feature representation is an evolution procedure of selecting the most effective subset of ordinal measures from the huge feature space. Our recent work [23] proposes a novel machine learning algorithm, Similarity-Oriented Boosting, to select multiple regional ordinal measures, achieving better iris recognition performance than state-of-the-art algorithms.

4.5 Iris database retrieval

In state-of-the-art iris recognition systems, the input iris image has to be compared with a large number of templates in database. When the scale of iris database increases, they are much less efficient and accurate. Possible solutions to speedup large-scale iris database retrieval are coarse classification of iris image database and image indexing technique. So the most similar templates to query iris image are chosen from central database for iris matching firstly.

We proposed a method for coarse iris classification based on occurrence of visual primitives in iris images [24]. Iris images in database are classified into five categories with a correct classification rate of 95%. By combining this method with traditional iris recognition algorithm, our system shows better performance in terms of both speed and accuracy.

5. Conclusions

Iris recognition has a bright future but great efforts are required on smart user interface and intelligent recognition algorithms. Next-generation iris recognition respects Human as the center of design principles. To improve the usability of iris recognition, iris acquisition should reduce the constraints on the position and motion of users and iris recognition algorithms should be more accurate and robust in iris localization, normalization and feature representation, secure in iris liveness detection and faster in iris database retrieval. This paper presents the technology roadmap of smart iris recognition, clarifying the unknown future, illustrating the evolution process, identifying the key problems, and providing possible solutions. Researchers, enterprisers, and investors in iris recognition can benefit from this paper to make right decisions, so that widespread usage of iris recognition to safeguard our society can be earlier realized.

6. References

[1] A. Jain, R. Bolle, and S. Pankanti, Biometrics: Personal Identification in a Networked Society, Kluwer, Norwell, 1999.

[2] Acuity Market Intelligence, The Future of Biometrics, http://www.acuity-mi.com/, 2007.

[3] CASIA Iris Image Database, http://www.cbsr.ia.ac.cn/irisdatabase.htm.

[4] T. Mansfield, G. Kelly, D. Chandler, and J. Kane, Biometric Product Testing Final Report, issue 1.0, National Physical Laboratory of UK, 2001.

[5] David Braun, How They Found National Geographic's "Afghan Girl", National Geographic News, March 7, 2003.

[6] L. Flom and A. Safir, “Iris Recognition System,” U.S. Patent, no. 4641394, 1987.

[7] http://www.panasonic.com/business/security/biometrics.asp

[8] http://www.lgiris.com

[9] Seiichi Itoda, Motomitsu Kikuchi, Seiichi Wada, Fully Automated Image Capturing-type Iris Recognition Device “IRISPASS-M”, Oki Technical Review, January 2006/Issue 205 Vol.73 No.1, pp.48-51.

[10] Craig Fancourt, Luca Bogoni, Keith Hanna, Yanlin Guo, Richard Wildes, Naomi Takahashi, and Uday Jain, Iris Recognition at a Distance, Proc. of AVBPA, Lecture Notes in Computer Science, Vol.3546, 2005, pp.1-13.

[11] Guodong Guo, Michael Jones and Paul Beardsley, "A System for Automatic Iris Capturing", Mitsubishi Electric Research Laboratories, TR2005-044, 2005.

[12] Wenbo Dong, Zhenan Sun, Tieniu Tan, Xianchao Qiu, “Self-adaptive iris image acquisition system”, Proc. of SPIE, Vol. 6944, 2008.

[13] J. Matey, O. Naroditsky, K. Hanna, et al., "Iris on the Move: Acquisition of Images for Iris Recognition in Less Constrained Environments", Proceedings of the IEEE, Vol.94, Issue 11, 2006, pp.1936-1947.

[14] Ellen Nakashima, "FBI Prepares Vast Database of Biometrics", Washington Post, December 22, 2007.

[15] J. Daugman, “High Confidence Visual Recognition of Persons by a Test of Statistical Independence”, IEEE Trans. Pattern Analysis and Machine Intelligence, Vol.15, No.11, pp.1148-1161, 1993.

[16] International Biometrics Group, “Independent Testing of Iris Recognition Technology”, Final Report, May 2005. http://www.biometricgroup.com/reports/public/ITIRT.html.

[17] Iris Challenge Evaluation, http://iris.nist.gov/ice/.

[18] John Daugman, "New Methods in Iris Recognition", IEEE TRANSACTIONS ON SYSTEMS, MAN, AND CYBERNETICS—PART B: CYBERNETICS, VOL. 37, NO. 5, OCTOBER 2007, pp.1167-1175.

[19] Zhuoshi Wei, Tieniu Tan, and Zhenan Sun, Nonlinear iris deformation correction based on Gaussian model, International Conference on Biometrics, Springer LNCS, Vol. 4642, pp. 780–789, Aug 2007.

[20] Lisa Thalheim, Jan Krissler, Peter-Michael Ziegler, "Body Check: Biometric Access Protection Devices and their Programs Put to the Test", c't 11/2002, page 114 - Biometrie. Available online http://www.heise.de/ct/english/02/11/114/.

[21] J. Daugman, "Recognizing Persons by Their Iris Patterns", in Biometrics: Personal Identification in Networked Society, A. K. Jain, R. Bolle, and S. Pankanti, editors, Kluwer Academic Publishers, 1999.

[22] Zhuoshi Wei, Xianchao Qiu, Zhenan Sun and Tieniu Tan, Texture classification towards anti-counterfeit iris image, Submitted to International Conference on Pattern Recognition, 2008.

[23] Zhaofeng He, Zhenan Sun, Wenbo Dong, Cheng Zhong, Tieniu Tan, Boosting Ordinal Features for Accurate and Fast Iris Recognition, IEEE International Conference on Computer Vision and Pattern Recognition, 2008.

[24] Xianchao Qiu, Zhenan Sun, and Tieniu Tan. Coarse Iris Classification by Learned Visual Dictionary. In Proc. of The 2nd International Conference on Biometrics, pages 770–779, Seoul, Korea, Aug. 2007.

About the author

Zhenan Sun is an assistant professor at Institute of Automation, Chinese Academy of Sciences. His contact email is znsun@nlpr.ia.ac.cn.

Wenbo Dong is a Ph.D. student at Institute of Automation, Chinese Academy of Sciences. His contact email is wbdong@nlpr.ia.ac.cn.

Tieniu Tan is a professor at Institute of Automation, Chinese Academy of Sciences. His contact email is tnt@nlpr.ia.ac.cn.

Table 1: Properties of iris image acquisition systems in SIR roadmap

Category	**Camera**	**Distance**	**Motion**	**User**	**Example systems**	**Applications**
Close-range IR	Passive	Close-range	Static	Single	BM-ET330 (Panasonic) [7], IrisAssess 4000 (LG) [8], CASIA-IrisCamV1	Access control, Time & Attendance, Banking, Personal security, etc.
Active IR	Active	Close-range	Static	Single	IRISPASS-M (OKI) [9], CASIA-IrisCamV2 [12]	
IR at a distance	Passive	Long-range	Static	Single	Iris at a Distance (Sarnoff) [10],	Pre- research for IR on move
Active IR at a distance	Active	Long-range	Static	Single	Mitsubishi [11], CASIA-IrisCamV3	
Passive IR on move	Passive	Long-range	Movement to an access control point	Single	Iris on Move (Sarnoff) [13]	Border-crossing, Airport, Stadium, Park, Hall, etc.
Active IR on move	Active	Long-range	Movement to an access control point	Single		
IR for Surveillance	Active	Long-range	Free movement	Multiple		Covert personal identification, Security surveillance, Watch-list, Homeland security, etc.

Vision-Simulated imaging

Brian A. Barsky
Computer Science Division and School of Optometry
University of California, Berkeley
Berkeley, CA 94720-1776
U.S.A.
barsky@cs.berkeley.edu

Abstract

Vision-simulated imaging (VSI) is the computer generation of synthetic images to simulate a subject's vision, by incorporating the characteristics of a particular individual's entire optical system. Using measured aberration data from a Shack-Hartmann wavefront aberrometry device, VSI modifies input images to simulate the appearance of the scene for the individual patient. Each input image can be a photograph, synthetic image created by computer, frame from a video, or standard Snellen acuity eye chart -- as long as there is accompanying depth information. An eye chart is very revealing, since it shows what the patient would see during an eye examination, and provides an accurate picture of his or her vision. Using wavefront aberration measurements, we determine a discrete blur function by sampling at a set of focusing distances, specified as a set of depth planes that discretize the three-dimensional space. For each depth plane, we construct an object-space blur filter. VSI methodology comprises several steps: (1) creation of a set of depth images, (2) computation of blur filters, (3) stratification of the image, (4) blurring of each depth image, and (5) composition of the blurred depth images to form a single vision-simulated image.

VSI provides images and videos of simulated vision to enable a patient's eye doctor to see the specific visual anomalies of the patient. In addition to blur, VSI could reveal to the doctor the multiple images or distortions present in the patient's vision that would not otherwise be apparent from standard visual acuity measurements. VSI could educate medical students as well as patients about the particular visual effects of certain vision disorders (such as keratoconus and monocular diplopia) by enabling them to view images and videos that are generated using the optics of various eye conditions. By measuring PRK/LASIK patients pre- and post-op, VSI could provide doctors with extensive, objective, information about a patient's vision before and after surgery. Potential candidates contemplating surgery could see simulations of their predicted vision and of various possible visual anomalies that could arise from the surgery, such as glare at night. The current protocol, where patients sign a consent form that can be difficult for a layperson to understand fully, could be supplemented by the viewing of a computer-generated video of simulated vision showing the possible visual problems that could be engendered by the surgery.

***Keywords**: vision realistic rendering**,** vision simulation, blur, optics, LASIK, PRK, corneal refractive surgery, cornea, visual acuity, visual performance, depth of field, optometry, ophthalmology, wavefront aberrometer, pupil, fovea.*

(left) Image simulating the vision of an aberration-free model eye. (right) Image simulating the vision of a patient with the vision disorder of keratoconus.

1. OPTOMETRY AND OPHTHALMOLOGY

In practice poor visual performance is often attributed to simple blur; however, our technique[1][2] enables the generation of vision-simulated images andanimations that demonstrate specific defects in how a person sees.Such images of simulated vision could be shown to an individual's eye care clinician toconvey the specific visual anomalies of the patient.Doctors and patients could be educated aboutparticular vision disorders by viewingimages that are generated using the opticsof various ophthalmic conditions such as*keratoconus*and *monocular diplopia*.

One of the most compelling applications is in the contextof vision correction using laser corneal refractive eye surgeries such asPRK (photorefractive keratectomy) and LASIK (laser in-situ keratomileusis).Currently, in the United States alone, a million people peryear choose to undergothis elective surgery.By measuring subjects pre-operatively and post-operatively,our technique could be used toconvey to doctors what the vision of a patient is like before and aftersurgery.In addition, accurate and revealing medical visualizations of predicted visual acuity andof simulated vision could be providedby using modeled or adjusted wavefront measurements.Potential candidates for such surgery could view these images to enable them tomake more educated decisions regarding the procedure.Still another application would be to show such candidatessome of the possible visualanomalies that could arise from the surgery, such as glare at night.With the increasing popularityof these surgeries, perhaps the current procedure which haspatients sign aconsent form that can be difficult for a layperson to understand fully could besupplemented by the viewing of a computer-generated animation ofsimulated visionshowing the possible visual problems that could be engendered by the surgery.

2. ALGORITHM

The approach comprises three major components, as follows:

2.1 Constructing Object Space Point Spread Function

A Point Spread Function (PSF) plots the distribution of light energy on theimage plane based on light that has emanated from a point source and haspassed through an optical system.Thus it can be used as an image space convolution kernel.

We introduce the object space point spread function (OSPSF), whichis similar to the usual image space point spread function, asdescribed above,except thatit is defined in object space and thus it varies with depth. The OSPSFis a continuous function of depth; however, wediscretize it, thereby defining a sequence of depthpoint spread functions (DPSF) at some chosen depths.

Since human blur discrimination is nonlinear in distancebut approximately linear in diopters (a unit measured in inverse meters),the depths are chosen with a constant dioptric spacing ΔDandthey range from the nearest depth of interest to the farthest. Atheoretical value of ΔD can be obtained from therelation $\Theta = p\Delta D$, where Θ is the minimum subtendedangle of resolution and p is thepupil size in meters. For a human with 20/20 visual acuity, Θis1 minute of arc; that is, $\Theta = 2.91 \times 10^{-4}$.

The DPSFs are histograms of rays cast normal to the wavefront. To compute these functions, we firstplace a grid with constant angular spacing at eachof the chosen depths and initialize counters in each grid cell to zero.Then we iteratively choose a point on the wavefront,calculate the normal direction, and cast a ray in this direction. Asthe ray passes through each grid, the cell it intersects has its counterincremented. This entireprocess is quite fast and millions of rays may be cast in a few minutes.Finally, we normalize the histogram so that its sum is unity.

In general, wavefront aberrations are measured with the subject's eyefocused at infinity.However, it is important to be able to shift focus for vision-simulated imaging.Recent research results in optometry showedthat aberrations change significantly with accommodation.When aberrometric data is available for the eye focused at the depththat will be used in the final image,our algorithm exploits that wavefront measurement.

In the situation where such data is not available, we assumethat the aberrations are independent ofaccommodation. We can then re-index the DPSFs, which is equivalent toshifting the OSPSF in the depth dimension.Note that this may require the computation of DPSFs at negative distances.

We further assume the OSPSF is independent of the image plane location.In optics,this is called the ``isoplanatic'' assumption and is the basis for beingable to perform convolutions across the visual field. For human vision,this assumption is valid for at least several degrees aroundthe fixation direction.

2.2 Fitting a Wavefront Surface to Aberrometry Data

The output of the Shack-Hartmann device comprisesa ray orientation (normal vector)at each lenslet. Current devices yield only 50 to 200 suchvectors. To generate the millions of samples necessary to calculate theOSPSF (see Section \ref{s:OSPSF} above), we first generate a smoothmathematical surface representation of the wavefront from this sparse data.Our wavefrontsurface is a fifth degree polynomial bivariate surface defined asa height field whose domain is the pupil plane.This surface is determined by a least squares fit to the Shack-Hartmann data.

We use a particular polynomial formwhich was developed in 1934 by the Dutch mathematician and physicistFrits Zernike who was awarded the Nobel Prize in Physics 1953 for discoveringthe phase contrastphenomenon.Zernike polynomials are derived from the orthogonalization of theTaylor series. The resulting polynomial basis corresponds toorthogonal wavefront aberrations. The coefficients weightingeach polynomial have easily derived relations with meaningfulparameters in optics.

2.3 Rendering Steps

Given the input image and its associated depth map,and the OSPSF, the vision-simulated imaging algorithm comprises three steps: (1) create a set of depth images,(2) blur each depth image, and (3) composite the blurred depth imagesto form a single vision-simulated image.

Create depth images:

Using the depth information, the image isseparated into a set of disjoint images, one at each of the depths chosen in thepreceding section. Ideally, the image at depth $d$would be rendered with thenear clipping plane set to $d+\Delta D/2$ and the far clipping plane set to$d-\Delta D/2$. Unfortunately, this is not possible becausewe are using previously rendered images and depth maps.Complicated texture synthesis algorithms would be overkill here,since the results will be blurred anyway.The following technique is simple, fast, and works well in practice:For each depth, d, those pixels from the original image that are within$\Delta D/2$ diopters of d are copied to the depth image.

Blur each depth image:

Once we have the depth images, we doa pairwise convolution: Each depth image is convolvedwith its corresponding DPSF, thereby producing aset of blurred depth images.

Composite:

Finally, we composite these blurred depth images into a single, vision-simulated image.This step is performed from far to near, using alpha-blendingfollowing alpha channel compositing rules.

2.4 Elimination of Occlusion and Discretization Artifacts

Although processing in image space allows an increase in speed, the imagesmay have artifacts introduced. This can occur in two ways, which we referto as *occlusion* and*discretization*. The occlusion problemarises because there is scene geometry that is missing. This resultsfrom the finite aperture of the lens, which allowsmore of the scene to be visiblethan would be seen through an infinitesimal pinhole.Thus, without additional input, the colors from parts of the scene that arebehind objects would have to be approximately reconstructed using the bordercolors of visible objects.

The discretization problem occurs fromseparating the image by depth. At adjacent pixels in different sub-images, thecalculation of depth of field is complicated. This arises because theseadjacentpixels may or may not correspond to the same object.An artifact can beintroduced into the image when a single object straddles twosub-images and the sub-images are blurred.The artifact arises when the far pixel is averaged with neighboring colorsbehind the near pixel that do not match the far pixel's color. Theneighboring colors are often black, which is the default backgroundcolor. Consequently, a black blurred band occurs at the intersectionof the object with the separation of the sub-images that it spans.

3. VALIDATION

An important area of future work is validation, and will involve the establishment of psychophysical experiments.

Nonetheless, some preliminary experiments are possible immediately, and our initial results have been positive. First, patients who haveunilateral vision problems can view our simulations of the visionin their pathological eye using their contralateral eye, thereby evaluating the fidelity of the simulation.

Second, consider patients who have vision conditions such as myopia, hyperopia, and astigmatism,that are completely corrected by spectacles or contact lenses.More precisely, in optometry terms, they might have 20/20 BSCVA (best spectacle corrected visual acuity). Such patients could validate thequality of the depiction of their vision in vision-simulated images simply by viewing them while wearing their corrective eyewear.Third, the visual anomalies present in keratoconus are different fromthose in more common conditions such as myopia, and this distinctionis indeed borne out in our example images. Specifically, keratoconuscan cause the appearance of diplopia (double-vision) whereas myopia.

4. CONCLUSION AND FUTURE WORK

We introduced the concept of *vision-simulated imaging* -- thecomputer generation of synthetic images that incorporate thecharacteristics of a particular individual's entire optical system.This paper took the first steps toward this goal, bydeveloping a method for simulating the scanned foveal image from wavefrontdata of actual human subjects, and demonstrated those methods on sample images.First, a subject's optical system is measured bya Shack-Hartmann wavefront aberrometry device. This device outputs ameasured wavefront which is sampled tocalculate an object space point spread function (OSPSF).The OSPSF isthen used to blur input images.This blurring is accomplished by creating a set of depth images,convolving them with the OSPSF, and finally compositingto form a vision-simulated image.Applications of vision-simulated imaging in computer graphics as well as in optometry and ophthalmologywere discussed.

The problem of vision-simulated imaging is by no means solved.Like early work on photo-realistic rendering, our method contains severalsimplifying assumptions and other limitations. There is muchinteresting research ahead.

The first limitationsare those stemming from the method of measurement. The Shack-Hartmanndevice, although capable of measuring a wide variety of aberrations, does nottake into account light scattering due to such conditions as cataracts.The wavefront measurements can have some error, and fitting the Zernikepolynomial surface to the wavefront data can introduce more. However,since the wavefronts from even pathological eyes tend to be continuous,smooth interpolation of the Shack-Hartmann data should not produce anysignificant errors. Consequently, any errors that are introducedshould be small and, furthermore, such small errors would imperceptiblein final images that have been discretized into pixels.

Strictly speaking, the pupil size used for vision-simulated imagingshould be the same as the pupil size when the measurements are taken.However, the error introduced in using only part of the wavefront(smaller pupil) or extrapolating the wavefront (larger pupil) shouldbe quite small. We have made use of three assumptions commonly usedin the study of human physiological optics: isoplanarity,independence of accommodation, and off-axis aberrations beingdominated by on-axis aberrations. Although we have argued that theseassumptions are reasonable and provide a good first-order approximation,a more complete model would remove at least the first two.

As discussed in Section 2.1, we have assumed"independence of accommodation" since aberrometric measurements with theeye focused at the depth is not usually available.However, this is not a limitation of our algorithm.Our algorithm can exploit wavefront data wherethe eye is focused at the depth that will be used in the final image,when such a measurement is made.

We currently do not take chromatic aberration into account, butagain that is not a limitation of our algorithm. Since the datawe acquire is from a laser, it is monochromatic. However, someresearch optometric colleagues have acquired polychromatic dataand will be sharing it with us. It is again interesting thatrecent research in optometry by Marcos [3] showed that except for the low orderaberrations, most aberrations are fairly constant over a range ofwavelengths.

We only compute the aberrations for one point in the fovea,and not for other points in the visual field. However, itis important to note that forcomputer graphics, the on-axis aberrations are criticallyimportant because viewers move their eyes around when viewing ascene. If we had actually included the off-axis aberrations ofthe eye, then the off-axis parts of the scene would have beenimproperly blurred for a person who is scanning the scene. Theoff-axis aberrations are of minor concern even without eyemovements since the retinal sampling of cones is sparse inperipheral vision. The image that we are simulating is formedby viewing the entire scene using the on-axis aberrations becausewe assume that the viewer is scanning the scene.

However, since peripheral vision does makes important contributions to visualappearance, viewers are affected by optical distortions of peripheral vision.Thus, it is of interest to extend this method to properly address theoff-axis effects.

REFERENCES

[1] Brian A. Barsky, Adam W. Bargteil, Daniel D. Garcia and Stanley A. Klein, "Introducing Vision-Realistic Rendering", Eurographics 2002 Poster Proceedings, Pisa, Italy, 26-28 June 2002, pp. 1-7.

[2] Brian A. Barsky, "Vision-Realistic Rendering: Simulation of the Scanned Foveal Image from Wavefront Data of Human Subjects",First Symposium on Applied Perception in Graphics and Visualization, co-located with ACM SIGGRAPH. Los Angeles, August 7-8 2004, pp. 73-81.

[3] Susana Marcos, Stephen A. Burns, Esther Moreno-Barriuso and Rafael Navarro, "A New Approach to the Study of Ocular Chromatic Aberrations", *Vision Research*, 1999, Vol. 39, pp. 4309-4323.

ACKNOWLEDGEMENTS

The author would like to thank Stanley A. Klein of the Vision Science Graduate Group at the University of California, Berkeley for his numerous contributions to this work.

About the author

Brian A. Barsky is a Professor of Computer Scienceand Affiliate Professor of Optometry at the University of California, Berkeley,

His contact email is barsky@cs.berkeley.edu and his personal webpage is: www.cs.berkeley.edu/~barsky.

FROM VIDEO-BASED EYETRACKING TO IMAGING BRAIN AND PERCEPTUAL CONSCIOUSNESS

Boris M. Velichkovsky

Institute of Cognitive Research, Kurchatov Research Centre, Moscow, and Department of Psychology, Dresden University of Technology, 01062 Dresden, Germany
velich@psychomail.tu-dresden.de

Recent progress in video-based eyetracking can be considered as a silent technological revolution in brain and behavioural sciences, approaching that of brain imaging methods. The importance of this methodology is quite obvious from the point of view of the ecological validity and practical implications of eyetracking. However, it is of a paramount significance for basic neurocognitive research as well. As a matter of fact, human eye movements are a common output of a number of philogenetically evolved and often (though not always) hierarchically organized brain systems. In this presentation, I will demonstrate how contemporary eyetracking research helps to disentangle their influences on task solution completing in a non-trivial way data obtained with neuroimaging methods.

Four groups of perceptual, cognitive and communicative tasks will be considered, with corresponding paradigms of eyetracking and neurocognitive studies. The first paradigm consists of the analysis of distractor influences on the duration of visual fixations during a free visual exploration of pictures. The second paradigm allows investigation of the role of attention in the process of perceiving static and dynamic visual scenes. The third investigates dissociations of the subjective focus of visual work and the physical location of visual fixations depending on the task at hand. Finally, the fourth paradigm is related to an analysis of the role of social gaze in processes of interpersonal communication. Up to five different brain systems seem to be at play in regulating parameters of eye movements in these experimental situations.

For instance, our habituation studies of distractor effect – a transient “freezing” of visual fixation in the actual position in response to a sudden optical event – reveals two completely different waves of saccadic inhibition at 90 and at 170 ms. Their origins could be tentatively identified with the superiour colliculus and the amygdala, respectively [1]. In a similar vein, two underlying systems seems to be at work in changing patterns of eye movement in the course of the exploration of static and particularly dynamic scenes such as VR simulation of hazardous traffic events. Indirect evidence helps us to identify the systems as the classical dorsal and ventral stream mechanisms of perceptual processing [2]. However we still lack direct confirmation of this caused by the low temporal resolution of most brain imaging methods. Comparable fMRI data exist in the case of social gaze studies (see [3]). Fig.1 illustrates the main effect contrasting a frontomedial and a (slight) right prefrontal activation during eye-to- eye contact with the predominantly parietal activation in an almost identical situation without such social gaze information. These prefrontal regions have been demonstrated to be involved in self-referential encoding [4, 5] while the posterior sites belong to the already mentioned dorsal stream structures. This is important in terms of

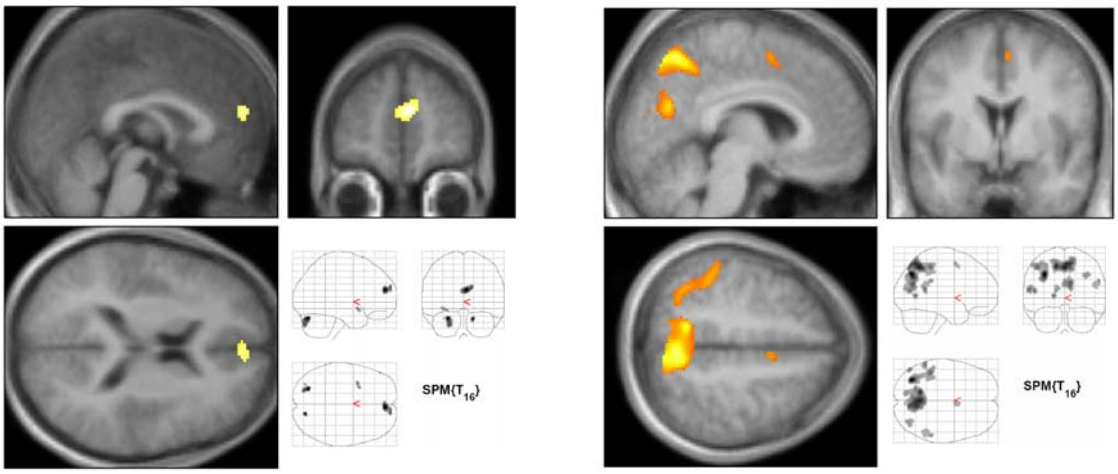

Fig.1 Typical BOLD-responses to the appearance of a virtual anthropomorphic agent looking either directly at the human observer (left) or at some imaginary location nearby of him/her (right)

the interpretation of the results. In addition, the data demonstrate that a single parameter of gaze direction in a social context can radically change the neurocognitive level of the information processing of the perceiver.

Current knowledge of the relationship between micro-behaviour of the human eye and the underlying brain processes allows new approaches to the visualisation of idiosyncratic individual perception. The first of these approaches, termed 'attentional landscapes method' [6], proposes a filtering of the visual scene in terms of the distribution of visual fixations. With the current differentiation of two modes of visual attention and their connection to ventral and dorsal streams it will be possible to reconstruct the subjective view of the situation as it is "seen" by more conscious ventral mechanisms of focal attention. Fig.2 illustrates another interesting aspect of this class of cognitively-motivated applications for eyetracking [7]. Here, attentional landscapes of expert and novice oncologists are compared while they are planning a neck dissection. Firstly, it is obvious that the distribution of focal attention in experts is much sharper – a feature we also observed in several other groups of experts, e.g. in cartography. Secondly and more importantly, through the measurement and rendering of such visualisations, thus far hidden personal views will become available for sharing with others, allowing enhanced and even entirely novel ways of communication, control and professional collaboration.

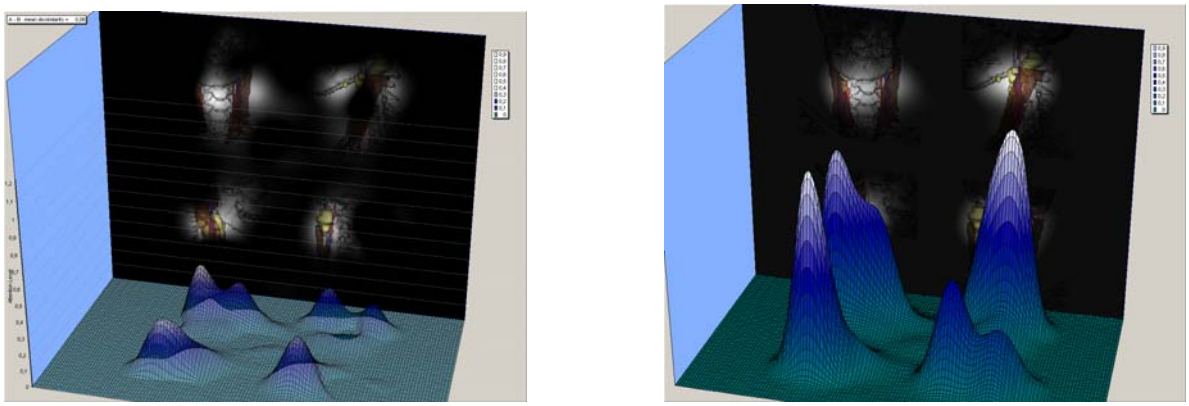

Fig. 2. Visualization of differences in conscious perception: novices *minus* experts (left), experts *minus* novices (right)

Acknowledgements

The work described in the talk has been supported by two grants of EU Commission under NEST-Pathfinder Program Measuring-the-Impossible (PERCEPT and MINET), by EU Network-of-Excellence COGAIN. I appreciate comments by Konstantin Anokhin, Oliver Burgert, Fiona Mulvey and Sebastian Pannasch to the ms.

References

1. S.-T. Graupner, B.M. Velichkovsky, S. Pannasch, and J. Marx, *Psychophysiology*, 2007, **44**(2), 251-261.
2. B.M. Velichkovsky, M. Joos, J.R. Helmert, and S. Pannasch, *Proc. 27th Conf. Cognitive Science Soc.*, Stresa, Italy, 2005, 2283-2288.
3. L. Schilbach, J.R. Helmert, A. Mojzisch, S. Pannasch, B.M. Velichkovsky, and K. Vogeley, *Proc. 1st Workshop Toward Social Mechanisms Android Science*, Stresa, Italy, 2005, 74-86.
4. B.M. Velichkovsky, T. Klemm, P.Dettmar, and H.-J. Volke, *Zeitschrift Elekroenzephalographie, Elektromyographie verwandte Gebiete*, 1996, **27**, 111-119.
5. F.I.M. Craik, T.M. Moroz, M. Moscovitch, D.T. Stuss, G. Winocur, E.Tulving, and S. Kapur, *Psychological Science*, 1999, **10**, 27-35.
6. B.M. Velichkovsky, M. Pomplun, and H. Rieser, *Visual attention and cognition.* W.H. Zangemeister, S. Stiel, and C.Freksa (Eds.). Amsterdam/New York: Elsevier, 1996, 125-154.
7. O. Burgert, V. Örn, B.M. Velichkovsky, M. Gessat, M. Joos, G. Strauß, C. Tietjen, B. Preim, I. Hertel, *SPIE Medical Imaging 2007, Proceedings of the SPIE*, Paper No. **6516-3**, San Diego, USA, 2007.

Decomposition of High Angular Resolution Diffusion Images into a Sum of Self-Similar Polynomials on the Sphere

Luc Florack* Evgeniya Balmashnova†
Eindhoven University of Technology, Department of Mathematics & Computer Science

Abstract

We propose a tensorial expansion of high resolution diffusion imaging (HARDI) data on the unit sphere into a sum of self-similar polynomials, i.e. polynomials that retain their form up to a scaling under the act of lowering resolution via the diffusion semigroup generated by the Laplace-Beltrami operator on the sphere. In this way we arrive at a hierarchy of HARDI degrees of freedom into contravariant tensors of successive ranks, each characterized by a corresponding level of detail. We provide a closed-form expression for the scaling behaviour of each homogeneous term in the expansion, and show that classical diffusion tensor imaging (DTI) arises as an asymptotic state of almost vanishing resolution.

CR Categories: I.4.10 [Computing Methodologies]: Image Representation—Multidimensional

Keywords: high angular resolution diffusion imaging (HARDI), diffusion tensor imaging (DTI), self-similar polynomials on the sphere

1 Introduction

High angular resolution diffusion imaging (HARDI) has become a popular magnetic resonance imaging (MRI) technique for imaging apparent water diffusion processes in fibrous tissues in vivo, such as brain white matter and muscle. Diffusion MRI is based on the assumption that Brownian motion of H_2O molecules is facilitated along the direction of fibers (axons or muscles). In classic diffusion tensor imaging (DTI), introduced by Basser et al. [Basser et al. 1994a; Basser et al. 1994b], cf. also Le Bihan et al. [Le Bihan et al. 2001], the diffusivity profile is modeled by a rank-2 contravariant diffusion tensor. Although the DTI representation is inherently limited by this restrictive assumption on the diffusivity profile, it does have the advantage that it enables one to view a spatial section of local diffusivity profiles as a (dual) Riemannian metric field. In turn, this view has led to the geometric rationale, in which fibers are modeled as (subsets of) geodesics induced by parallel transport under the corresponding metric connection [Astola et al. 2007; Fillard et al. 2007; Lenglet et al. 2004; Pennec et al. 2006; Prados et al. 2006]. Congruences of geodesics can be studied likewise in the geometric framework of Hamilton-Jacobi theory [Rund 1973], which has led to efficient algorithms for connectivity analysis (eikonal equation, fast marching schemes, and the like).

*e-mail: L.M.J.Florack@tue.nl
†e-mail: E.B.Balmashnova@tue.nl

For simplicity we use the term HARDI to collectively denote schemes that employ functions on the sphere, including Tuch's orientation distribution function (ODF) [Tuch 2004], the higher order diffusion tensor model and the diffusion orientation transform (DOT) by Özarslan et al. [Özarslan and Mareci 2003; Özarslan et al. 2006], Q-Ball imaging [Descoteaux et al. 2007], and the diffusion tensor distribution model by Jian et al. [Jian et al. 2007].

Because the general HARDI model accounts for arbitrarily complex diffusivity profiles, it raises a concomitant demand for regularization [Descoteaux et al. 2006; Descoteaux et al. 2007; Hess et al. 2006; Pennec et al. 2006; Tikhonov and Arseninn 1977], since there is no a priori smoothness of acquisition data. Indeed, in the context of regularization schemes, DTI can be seen as an asymptotic regularization of the actual diffusivity profile.

A natural way to combine the conceptual advantage of DTI (notably its connection to a Riemannian framework) with the superior data modeling capability of HARDI, is to consider a polynomial expansion of the diffusivity function on the sphere that can be likewise represented in terms of a contravariant rank-2 tensor field, which can then be used so as to obtain a generalized, orientation dependent Finsler metric [Melonakos et al. 2008]. A polynomial expansion of HARDI data on the sphere has been proposed previously by Özarslan and Mareci [Özarslan and Mareci 2003]. However, these authors consider a *homogeneous* expansion, containing terms of some *fixed* order only. They point out that any (again homogeneous) model of lower order can be obtained in analytically closed form from the result, i.e. without the need for a data refit. This is true, and indeed a sensible approach, since (even/odd) monomials of fixed order, N say, confined to the unit sphere, can be linearly combined so as to produce any lower order (even/odd) monomial by virtue of the radial constraint $r = 1$ of the unit sphere embedded in Euclidean n-space (in our case, $n = 3$).

However, in this paper we propose an *inhomogeneous* expansion, including all (even) orders up to some fixed N, and exploit the redundancy of such a representation. (Odd terms are of no interest, as the HARDI profile is assumed to be symmetric.) The idea is to construct a polynomial on the sphere in such a way that the higher order terms capture *residual* information of the HARDI profile only, i.e. the additional structure that cannot be revealed by a lower order polynomial. As such the polynomial expansion can in theory be continued to a series expansion of infinite order. We construct this polynomial representation order by order, in such a way that adding a higher order term does not affect already established lower order terms. As a consequence the information in the HARDI data is distributed hierarchically over diffusion tensor coefficients of all ranks.

The polynomial representation admits regularization. This provides control over complexity and angular resolution. Above all, it reveals the data hierarchy alluded to above, in the sense that the collective terms of fixed order are self-similar under canonical resolution degradation induced by the Laplace-Beltrami operator on the sphere (cf. Koenderink for a physical motivation of this paradigm in the Euclidean setting [Koenderink 1984]), with a characteristic decay that depends on order. In this sense they constitute the tensorial counterparts of the canonical eigensystem of spherical harmonics with corresponding discrete spectrum.

Finally, we point out the explicit relationship between HARDI and DTI via asymptotic regularization. This is of interest, as it permits one to extend and apply established geometric techniques for connectivity analysis and tractography that have been successfully used in the context of classical rank-2 DTI.

2 Theory

We consider the unit sphere embedded in Euclidean 3-space, given in terms of the vector components g^i, $i = 1, \ldots, n$ (with $n = 3$ in our application of interest):

$$\eta_{ij}\, g^i\, g^j = 1\,. \tag{1}$$

Einstein summation convention applies to pairs of identical upper and lower indices. The components of the Euclidean metric and corresponding dual metric of the embedding space are given by η_{ij}, respectively η^{ij}, with the help of which indices can be lowered or raised. We have, for instance[1], $g_i = \eta_{ij}\, g^j$, the dual covector components corresponding to g^i. The corresponding analogue of Eq. (1) is therefore

$$\eta^{ij}\, g_i\, g_j = 1\,. \tag{2}$$

In Cartesian coordinates we have $\eta_{ij} = \eta^{ij} = 1$ iff $i = j$ for $i, j = 1, \ldots, n$, otherwise 0, so that Eq. (2) reduces to $g_1^2 + g_2^2 + g_3^2 = 1$, and similarly for the vectorial representation, Eq. (1).

The Riemannian metric of the embedded unit sphere is given in terms of the components

$$g_{\mu\nu} = \frac{\partial g^i}{\partial \xi^\mu} \eta_{ij} \frac{\partial g^j}{\partial \xi^\nu}\,, \tag{3}$$

in which ξ^μ ($\mu = 1, \ldots, n-1$) parameterize the sphere. Recall that the canonical parametrization of the sphere in terms of the usual polar angles, $(\theta, \phi) \in [0, \pi] \times [0, 2\pi)$, is as follows:

$$\Omega : \left\{ \begin{array}{lcl} g^1 & = & \sin\theta \cos\phi\,, \\ g^2 & = & \sin\theta \sin\phi\,, \\ g^3 & = & \cos\theta\,. \end{array} \right. \tag{4}$$

The corresponding measure is abbreviated by $dg = \sin\theta\, d\theta\, d\phi$.

We consider a higher order DTI representation of the form

$$D(g) = \sum_{k=0}^{\infty} D^{i_1 \ldots i_k}\, g_{i_1} \ldots g_{i_k}\,. \tag{5}$$

(Under the stipulated symmetry, $D(g) = D(-g)$, only even orders will be of interest.) The collection of polynomials on the sphere,

$$\mathscr{B} = \bigcup_{k \in \mathbb{N} \cup \{0\}} \mathscr{B}_k\,, \tag{6}$$

spanned by the monomial subsets

$$\mathscr{B}_k = \{ g_{i_1} \ldots g_{i_k} \mid k \in \mathbb{N} \cup \{0\} \text{ fixed} \}\,, \tag{7}$$

is complete, but redundant. Apart from the fact that odd order monomials are of no interest, redundancy is evident from the fact that lower order even monomials can be reproduced from higher order ones through contractions as a consequence of the quadratic constraint that defines the embedded unit sphere, recall Eq. (2). As a result, we have, e.g.,

$$g_{i_1} \ldots g_{i_k} = \eta^{i_{k+1} i_{k+2}}\, g_{i_1} \ldots g_{i_{k+2}}\,, \tag{8}$$

[1]The covector model reflects the physical nature of the components as normalized diffusion sensitizing gradients, i.e. covectors.

and, by recursion, we find similar dependencies for all lower order monomials in terms of higher order ones. Thus any monomial of order $k \leq N \in \mathbb{N} \cup \{0\}$ is linearly dependent on the set of N-th order monomials of equal (even/odd) parity. This, of course, justifies the approach by Özarslan and Mareci [Özarslan and Mareci 2003], in which the data are fitted only against linear combinations of N-th order monomials, discarding all lower order terms. In particular, the larger N is, the better the approximation of the data will be. However, in the process of updating N, all HARDI data information will migrate to the tensor coefficients of corresponding rank. The reader is referred to the seminal paper by Özarslan and Mareci [Özarslan and Mareci 2003] for further details and physical background.

Still, it is not necessary to employ a basis of fixed order monomials. One can actually exploit the redundancy in $\mathscr{B}$, Eq. (6). For instance, we have

$$\mathscr{F}_N = \left(\begin{array}{c} N+2 \\ N \end{array} \right) \tag{9}$$

independent N-th order basis monomials due to symmetry, as opposed to $N!$ for an arbitrary rank-N tensor. It also follows that $\mathscr{F}_N$ is in fact the exact number of degrees of freedom of our full N-th order polynomial expansion, i.e. including all monomials of orders less than N. Consequently, if we retain all lower order monomials, it follows from Eq. (8) that the *effective* number of independent degrees of freedom in our N-th order term must be lower than $\mathscr{F}_N$, recall Eq. (9), viz. equal to the number of independent components of the symmetric rank-N tensor minus the number of degrees of freedom already contained in the lower order terms:

$$\mathscr{F}_N^{\text{residual}} = \mathscr{F}_N - \mathscr{F}_{N-2} = 2N + 1\,. \tag{10}$$

This number therefore corresponds to the dimensionality of the residual degrees of freedom. If, in case of even N, we count all spherical harmonics Y_ℓ^m for even $\ell = N, N-2, \ldots, 0$, and all $m \in \{-\ell, \ldots, \ell\}$—let us call this number $\mathscr{G}_N$—then we reobtain Eq. (9), since

$$\mathscr{G}_N = \sum_{\ell=0\,,\ell \text{ even}}^{N} (2\ell + 1) = \frac{(N+1)(N+2)}{2} = \mathscr{F}_N\,. \tag{11}$$

(The same result holds for N odd, in which case summation should be restricted to odd ℓ-values only, but this is not relevant for us.) Notice that, in particular, the number of independent degrees of freedom of the spherical harmonics of order N, $\mathscr{G}_N^{\text{residual}}$ say, likewise equals

$$\mathscr{G}_N^{\text{residual}} = \mathscr{G}_N - \mathscr{G}_{N-2} = 2N + 1 = \mathscr{F}_N^{\text{residual}}\,. \tag{12}$$

These counting arguments suggest an intimate relationship between the rank-k tensor coefficients of Eq. (5) in our scheme, v.i., and the spherical harmonics of order k.

Model redundancy may be beneficial, to the extent that it enables us to distribute the HARDI degrees of freedom *hierarchically* over the various orders involved, in such a way that only residual information is encoded in the higher order tensor coefficients. As $N \to \infty$ this residual tends to zero, while all established tensor coefficients of lower rank than N remain fixed in the process of incrementing N. (The hierarchy implicit in Özarslan and Mareci's scheme is of a different nature.) We return to the potential benefit of our inhomogeneous polynomial expansion below.

We construct the coefficients as follows. Suppose we are in possession of $D^{i_1 \ldots i_k}$ for all $k = 0, \ldots, N-1$, then we consider the

function

$$E_N(D^{j_1\cdots j_N}) = \int \left(D(g) - \sum_{k=0}^{N} D^{i_1\ldots i_k} g_{i_1}\ldots g_{i_k} \right)^2 dg\,, \tag{13}$$

and find the N-th order coefficients by minimization. Setting

$$\frac{\partial E_N(D^{j_1\cdots j_N})}{\partial D^{i_1\ldots i_N}} = 0\,, \tag{14}$$

one obtains the following linear system:

$$\Gamma_{i_1\ldots i_N j_1\ldots j_N} D^{j_1\cdots j_N} = \int D(g)\, g_{i_1}\ldots g_{i_N}\, dg - \sum_{k=0}^{N-1} \Gamma_{i_1\ldots i_N j_1\ldots j_k} D^{j_1\cdots j_k}\,, \tag{15}$$

with symmetric covariant tensor coefficients

$$\Gamma_{i_1\ldots i_k} = \int g_{i_1}\ldots g_{i_k}\, dg\,. \tag{16}$$

The appearance of the second inhomogeneous term on the r.h.s. of Eq. (15), absent in the scheme proposed by Özarslan and Mareci, reflects the fact that in our scheme higher order coefficients encode residual information only.

It is immediately evident that

$$\Gamma_{i_1\ldots i_{2k+1}} = 0 \quad (k \in \mathbb{N}\cup\{0\})\,, \tag{17}$$

since no odd-rank tensors with covariantly constant coefficients exist. All even-rank tensors of this type must be products of the Euclidean metric tensor, so we stipulate

$$\Gamma_{i_1\ldots i_{2k}} = \gamma_k\, \eta_{(i_1 i_2}\ldots\eta_{i_{2k-1}i_{2k})}\,, \tag{18}$$

for some constant γ_k. Parentheses denote index symmetrization. The constant γ_k needs to be determined for each $k \in \mathbb{N}\cup\{0\}$.

One way to determine γ_k is to perform a full contraction of indices in Eq. (18), which, with the help of Eqs. (2) and (16), yields

$$\gamma_k = \frac{\Gamma}{\eta_{(i_1 i_2}\ldots\eta_{i_{2k-1}i_{2k})}\,\eta^{i_1 i_2}\ldots\eta^{i_{2k-1}i_{2k}}}\,. \tag{19}$$

To find the denominator on the r.h.s. is an exercise in combinatorics [Grimaldi 1993], and requires the basic trace property $\eta_{ij}\eta^{ij} = \delta_i^i = n$. A simpler way to find γ_k is to evaluate Eq. (18) for $i_1 = \ldots = i_{2k} = 1$ in a Cartesian coordinate system, since the symmetric product of metric tensors on the r.h.s. evaluates to 1 for this case:

$$\gamma_k = \Gamma_{1\ldots\leftarrow 2k \text{ indices}\rightarrow\ldots 1} = \int g_1^{2k}\, dg\,. \tag{20}$$

This integral is a special case of the closed-form multi-index representation of Eq. (16), cf. Folland [Folland 2001] and Johnston [Johnston 1960], viz.:

$$\int g_1^{\alpha_1}\ldots g_n^{\alpha_n}\, dg = \frac{2}{\Gamma(\frac{1}{2}|\alpha| + \frac{n}{2})} \prod_{i=1}^{n} \Gamma(\frac{1}{2}\alpha_i + \frac{1}{2})\,, \tag{21}$$

if all α_j are even (otherwise the integral vanishes). Here $|\alpha| = \alpha_1 + \ldots + \alpha_n = 2k$ denotes the norm of the multi-index, and

$$\Gamma(t) = \int_0^\infty s^{t-1}\, e^{-s}\, ds = 2\int_0^\infty r^{2t-1}\, e^{-r^2}\, dr \tag{22}$$

is the gamma function. Recall $\Gamma(\ell) = (\ell-1)!$ and $\Gamma(\ell+\frac{1}{2}) = (\ell-\frac{1}{2})\ldots\frac{1}{2}\sqrt{\pi} = (2\ell)!\sqrt{\pi}/(4^\ell\,\ell!)$ for non-negative integers $\ell \in \mathbb{N}\cup\{0\}$. For the specific monomial in Eq. (20) we have $\alpha = (2k, 0, \ldots, 0) \in \mathbb{Z}^n$.

Result 1 *Recall Eqs. (16–18). For general n we have*

$$\gamma_k = \frac{2\,\Gamma(k+\frac{1}{2})\Gamma(\frac{1}{2})^{n-1}}{\Gamma(k+\frac{n}{2})}\,,$$

in other words,

$$\Gamma_{i_1\ldots i_{2k}} = \frac{2\,\Gamma(k+\frac{1}{2})\Gamma(\frac{1}{2})^{n-1}}{\Gamma(k+\frac{n}{2})}\,\eta_{(i_1 i_2}\ldots\eta_{i_{2k-1}i_{2k})}\,.$$

For $n = 3$ in particular, we obtain

$$\gamma_k = \frac{2\pi}{k+\frac{1}{2}}\,,$$

whence

$$\Gamma_{i_1\ldots i_{2k}} = \frac{2\pi}{k+\frac{1}{2}}\,\eta_{(i_1 i_2}\ldots\eta_{i_{2k-1}i_{2k})}\,.$$

This result is the tensorial counterpart of Eq. (21). Some examples ($n = 3$):

$$\begin{aligned} k=0 \;:\; \Gamma &= 4\pi \\ k=1 \;:\; \Gamma_{ij} &= \frac{4\pi}{3}\,\eta_{ij} \\ k=2 \;:\; \Gamma_{ijk\ell} &= \frac{4\pi}{15}\,(\eta_{ij}\,\eta_{k\ell} + \eta_{ik}\,\eta_{j\ell} + \eta_{i\ell}\,\eta_{jk})\,. \end{aligned}$$

The corresponding linear systems, recall Eq. (15), are as follows:

$$\begin{aligned} \Gamma\, D &= \int D(g)\, dg\,, \\ \Gamma_{ij}\, D^j &= \int D(g)\, g_i\, dg - \Gamma_i\, D\,, \\ \Gamma_{ijk\ell} D^{k\ell} &= \int D(g)\, g_i\, g_j\, dg - \Gamma_{ij}\, D - \Gamma_{ijk}\, D^k\,. \end{aligned}$$

It follows that the scalar constant D is just the average diffusivity over the unit sphere:

$$D = \frac{\int D(g)\, dg}{\int dg}\,. \tag{23}$$

The constant vector D^i vanishes identically, as it should. For the rank-2 tensor coefficients we find the traceless matrix

$$D_{ij} = \frac{15\int D(g)\, g_i\, g_j\, dg - 5\int D(g)\, dg\, \eta_{ij}}{2\int dg}\,, \tag{24}$$

and so forth. If, instead, we fit a homogeneous second order polynomial to the data (by formally omitting the second term on the r.h.s. of Eq. (15)), as proposed by Özarslan and Mareci, we obtain the following rank-2 tensor coefficients:

$$D_{ij}^{\text{Ö.M.}} = \frac{15\int D(g)\, g_i\, g_j\, dg - 3\int D(g)\, dg\, \eta_{ij}}{2\int dg}\,, \tag{25}$$

which is clearly different. However, Özarslan and Mareci's homogeneous polynomial expansion should be compared to our inhomogeneous expansion. Indeed, if we compare the respective second order expansions in this way we observe that $D_2^{\text{Ö.M.}}(g) = D_2(g)$. The difference in coefficients, in this example, is explained by the contribution already contained in the lowest order term of our polynomial, which in Özarslan and Mareci's scheme has to migrate to the second order tensor.

In general we raise the conjecture that to any order N we have equality.

Theorem 1 *Let $D_N(g)$ denote the truncated expansion of Eq. (5) including monomials of orders $k \leq N$ only, and let $D_N^{\ddot{O}.M.}(g)$ denote the N-th order homogeneous polynomial expansion proposed by Özarslan and Mareci, loc. cit., then*

$$D_N^{\ddot{O}.M.}(g) = D_N(g)\,.$$

However, the interesting claim we wish to make is the following, which shows exactly what we mean by the hierarchical ordering of degrees of freedom in our inhomogeneous expansion:

Theorem 2 *If Δ denotes the Laplace-Beltrami operator on the unit sphere, then for any $N \in \mathbb{N} \cup \{0, \infty\}$*

$$D_N(g,t) \equiv e^{t\Delta}\, D_N(g) = \sum_{k=0}^{N} D^{i_1 \dots i_k}(t)\, g_{i_1} \dots g_{i_k}\,,$$

with

$$D^{i_1 \dots i_k}(t) = e^{-k(k+1)t}\, D^{i_1 \dots i_k}\,.$$

For brevity we set $D(g,t) = D_\infty(g,t)$.

This is nontrivial, since the monomials $g_{i_1} \dots g_{i_n}$ are themselves not eigenfunctions of the Laplace-Beltrami operator. The construction of the coefficients in the linear combinations as they occur in the inhomogeneous expansion, implicitly defined by Eq. (15), is apparently crucial. For instance, the scaling of the second order term in Theorem 2 is a direct consequence of the fact that the coefficient matrix in Eq. (24) is traceless, as opposed to Eq. (25).

Proof of Theorems 1–2. Consider the following closed linear subspace of $L_2(\Omega)$ for even N:

$$X_N = \text{span}\,\{g_{i_1} \dots g_{i_N}\} = \bigoplus_{k=0}^{N/2} S_{2k}\,,$$

in which $S_{2k} = \text{span}\,\{Y_{2k}^m \,|\, m = -2k, -2k+1, \dots 2k-1, 2k\}$. Set $\phi_N(g) = D(g) - D_{N-2}(g)$, with induction hypothesis $P_{S_{2k}}\phi_N = 0$ for all $k = 0, \dots, N/2-1$, in which $P_{S_{2k}}$ denotes orthogonal projection onto S_{2k}. In other words, by hypothesis,

$$\phi_N \in \bigoplus_{k=N/2}^{\infty} S_{2k}\,.$$

Let $\psi_N \in X_N$ be such as to minimize $E(\psi) = \|\phi_N - \psi\|_{L_2(\Omega)}$ for $\psi \in X_N$. Obviously $P_{S_N}\phi_N \in X_N$, so that by definition of ψ_N we obtain

$$\|\phi_N - \psi_N\|_{L_2(\Omega)} \leq \|\phi_N - P_{S_N}\phi_N\|_{L_2(\Omega)}\,.$$

On the other hand, since $\phi_N - P_{S_N}\phi_N \perp P_{S_N}\phi_N - \psi_N$, we also have

$$\begin{aligned}\|\phi_N - \psi_N\|^2_{L_2(\Omega)} &= \|\phi_N - P_{S_N}\phi_N + P_{S_N}\phi_N - \psi_N\|^2_{L_2(\Omega)} = \\ &\|\phi_N - P_{S_N}\phi_N\|^2_{L_2(\Omega)} + \|P_{S_N}\phi_N - \psi_N\|^2_{L_2(\Omega)} \\ \geq\ &\|\phi_N - P_{S_N}\phi_N\|^2_{L_2(\Omega)}\,.\end{aligned}$$

We conclude that

$$\|\phi_N - \psi_N\|_{L_2(\Omega)} = \|\phi_N - P_{S_N}\phi_N\|_{L_2(\Omega)}\,,$$

in other words, $\psi_N = P_{S_N}\phi_N$, so that apparently $\psi_N \in S_N$. Note that S_k is precisely the degenerate eigenspace of the Laplace-Beltrami operator, Δ, with corresponding eigenvalue $-k(k+1)$, whence the eigenvalue of $\exp(t\Delta)$ equals $\exp(-k(k+1)t)$. This completes the proof. □

The significance of Theorem 2 is that it segregates degrees of freedom in the polynomial expansion in such a way that we may interpret each homogeneous higher order term as an incremental refinement of detail relative to that of the lower order expansion. To see this, note that $D_N(g,t)$ satisfies the heat equation on the unit sphere, recall Eq. (3):

$$\frac{\partial u}{\partial t} = \frac{1}{\sqrt{g}}\,\partial_\mu\left(g^{\mu\nu}\sqrt{g}\partial_\nu u\right) = \Delta u\,, \tag{26}$$

in which the initial condition corresponds to the N-th order expansion of the raw data, $D_N(g,0) = D_N(g)$. Recall that in the usual polar coordinates in $n = 3$ dimensions we have for a scalar function on the unit sphere:

$$\Delta u(\theta,\phi) = \left(\frac{1}{\sin^2\theta}\frac{\partial^2}{\partial\phi^2} + \frac{1}{\sin\theta}\frac{\partial}{\partial\theta}\left(\sin\theta\frac{\partial}{\partial\theta}\right)\right) u(\theta,\phi)\,. \tag{27}$$

The remarkable fact is thus that the linear combinations $D^{i_1\dots i_k}\, g_{i_1}\dots g_{i_k}$, unlike the monomials $g_{i_1}\dots g_{i_k}$ separately, are eigenfunctions of the heat operator $\exp(t\Delta)$, i.e. *self-similar polynomials on the sphere*, which admit a reformulation in terms of purely k-th order spherical harmonics, with eigenvalues $e^{-k(k+1)t}$. The heat operator can be seen as the canonical resolution degrading semigroup operator [Koenderink 1984; Florack 1997]. The parameter t denotes the (square of) angular scale, or inverse resolution, at which the raw data are resolved. Indeed, the classical rank-2 DTI representation, defined via the Stejskal-Tanner formula [Özarslan and Mareci 2003; Stejskal and Tanner 1965]:

$$S(g) = S_0 \exp\left(-bD(g)\right)\,, \tag{28}$$

arises not merely as an approximation under the assumption that the diffusion attenuation can be written as

$$D(g) \approx D_{\text{DTI}}(g) = D^{ij}_{\text{DTI}}\, g_i\, g_j\,, \tag{29}$$

but expresses the *exact* asymptotic behaviour of $D(g,t)$ as $t \to \infty$, recall Eq. (2) and Theorem 2:

$$D(g,t) = \underbrace{\left(D\,\eta^{ij} + e^{-6t}\,D^{ij}\right)\, g_i\, g_j}_{D_{\text{DTI}}(g,t)\,=\,D^{ij}_{\text{DTI}}(t)\,g_i\,g_j} + \mathcal{O}(e^{-12t}) \quad (t \to \infty)\,. \tag{30}$$

It shows that the DTI tensor is not self-similar, but has a bimodal resolution dependence. The actual limit of truly vanishing resolution is of course given by a complete averaging over the sphere:

$$\lim_{t\to\infty} D(g,t) = \lim_{t\to\infty} D_{\text{DTI}}(g,t) = D\,, \tag{31}$$

recall Eq. (23). See Figs. 1–2 for an illustration of Theorem 2 for $N = 8$ on a synthetic image with Rician noise.

3 Conclusion

We have proposed a tensorial representation of high angular resolution diffusion images (HARDI), or derived functions defined on the unit sphere, in terms of a family of inhomogeneous polynomials on the sphere. The resulting polynomial representation, truncated at some arbitrary order, or formally extended into an infinite series, may be regarded as the canonical way of decomposing HARDI data into "higher order diffusion tensors", to the extent that the successive homogeneous terms capture residual information only, i.e. degrees of freedom that cannot be detailed by a lower order expansion. In this sense they form the tensorial counterpart of the spherical harmonic decomposition. A related consequence is that the inhomogeneous polynomial expansion neatly segregates the HARDI signal

into a hierarchy of homogeneous polynomials that are *self-similar* under the act of graceful resolution degradation induced by heat operator, $\exp(t\Delta)$, generated by the isotropic Laplace-Beltrami operator Δ on the sphere, with a characteristic decay that depends on order (for fixed $t \in \mathbb{R}^+$). The asymptotic case of almost vanishing resolution ($t \to \infty$) reproduces the diffusion tensor of classical diffusion tensor imaging (DTI), with one constant and one resolution-dependent mode. The true asymptotic case leads to a complete averaging over the sphere, as expected. The general N-th order expansion provides control over the trade-off between regularity (choice of t) and complexity (choice of N), i.e. descriptive power. Finally, we have related our result to the homogeneous polynomial expansion proposed by Özarslan and Mareci [Özarslan and Mareci 2003], and argued that the expansions lead to identical results despite the differences in coefficients. We have stressed the fact that this is possible by virtue of the redundancy inherent in the use of an inhomogeneous polynomial representation.

Acknowledgements

The Netherlands Organisation for Scientific Research (NWO) is gratefully acknowledged for financial support. We thank Erwin Vondenhoff and Mark Peletier for a fruitful discussion, and Vesna Prckovska for implementations and illustrations.

The invitation and financial support by Andrey Krylov, Moscow Lomonosov State University, is greatly appreciated.

References

ASTOLA, L., FLORACK, L., AND TER HAAR ROMENY, B. 2007. Measures for pathway analysis in brain white matter using diffusion tensor images. In *Proceedings of the Fourteenth International Conference on Information Processing in Medical Imaging–IPMI 2007 (Kerkrade, The Netherlands)*, Springer-Verlag, Berlin, N. Karssemeijer and B. Lelieveldt, Eds., vol. 4584 of *Lecture Notes in Computer Science*, 642–649.

BASSER, P. J., MATTIELLO, J., AND LE BIHAN, D. 1994. Estimation of the effective self-diffusion tensor from the NMR spin echo. *Journal of Magnetic Resonance 103*, 247–254.

BASSER, P. J., MATTIELLO, J., AND LE BIHAN, D. 1994. MR diffusion tensor spectroscopy and imaging. *Biophysics Journal 66*, 1, 259–267.

DESCOTEAUX, M., ANGELINO, E., FITZGIBBONS, S., AND DERICHE, R. 2006. Apparent diffusion coefficients from high angular resolution diffusion imaging: Estimation and applications. *Magnetic Resonance in Medicine 56*, 395–410.

DESCOTEAUX, M., ANGELINO, E., FITZGIBBONS, S., AND DERICHE, R. 2007. Regularized, fast, and robust analytical Q-ball imaging. *Magnetic Resonance in Medicine 58*, 497–510.

FILLARD, P., PENNEC, X., ARSIGNY, V., AND AYACHE, N. 2007. Clinical DT-MRI estimation, smoothing, and fiber tracking with log-Euclidean metrics. *IEEE Transactions on Medical Imaging 26*, 11 (November).

FLORACK, L. M. J. 1997. *Image Structure*, vol. 10 of *Computational Imaging and Vision Series*. Kluwer Academic Publishers, Dordrecht, The Netherlands.

FOLLAND, G. B. 2001. How to integrate a polynomial over a sphere. *The American Mathematical Monthly 108*, 5 (May), 446–448.

GRIMALDI, R. P. 1993. *Discrete and Combinatorial Mathematics: An Applied Introduction*. Addison-Wesley, Boston, MA, USA.

HESS, C. P., MUKHERJEE, P., TAN, E. T., XU, D., AND VIGNERON, D. B. 2006. Q-ball reconstruction of multimodal fiber orientations using the spherical harmonic basis. *Magnetic Resonance in Medicine 56*, 104–117.

JIAN, B., VEMURI, B. C., ÖZARSLAN, E., CARNEY, P. R., AND MARECI, T. H. 2007. A novel tensor distribution model for the diffusion-weighted MR signal. *NeuroImage 37*, 164–176.

JOHNSTON, T. W. 1960. Cartesian tensor scalar product and spherical harmonic expansions in Boltzmann's equation. *Physical Review 120*, 1103–1111.

KOENDERINK, J. J. 1984. The structure of images. *Biological Cybernetics 50*, 363–370.

LE BIHAN, D., MANGIN, J.-F., POUPON, C., CLARK, C. A., PAPPATA, S., MOLKO, N., AND CHABRIAT, H. 2001. Diffusion tensor imaging: Concepts and applications. *Journal of Magnetic Resonance Imaging 13*, 534–546.

LENGLET, C., DERICHE, R., AND FAUGERAS, O. 2004. Inferring white matter geometry from diffusion tensor MRI: Application to connectivity mapping. In *Proceedings of the Eighth European Conference on Computer Vision (Prague, Czech Republic, May 2004)*, Springer-Verlag, Berlin, T. Pajdla and J. Matas, Eds., vol. 3021–3024 of *Lecture Notes in Computer Science*, 127–140.

MELONAKOS, J., PICHON, E., ANGENENT, S., AND TANNENBAUM, A. 2008. Finsler active contours. *IEEE Transactions on Pattern Analysis and Machine Intelligence 30*, 3, 412–423.

ÖZARSLAN, E., AND MARECI, T. H. 2003. Generalized diffusion tensor imaging and analytical relationships between diffusion tensor imaging and high angular resolution imaging. *Magnetic Resonance in Medicine 50*, 955–965.

ÖZARSLAN, E., SHEPHERD, T. M., VEMURI, B. C., BLACKBAND, S. J., AND MARECI, T. H. 2006. Resolution of complex tissue microarchitecture using the diffusion orientation transform (DOT). *NeuroImage 31*, 1086–1103.

PENNEC, X., FILLARD, P., AND AYACHE, N. 2006. A Riemannian framework for tensor computing. *International Journal of Computer Vision 66*, 1 (January), 41–66.

PRADOS, E., SOATTO, S., LENGLET, C., PONS, J.-P., WOTAWA, N., DERICHE, R., AND FAUGERAS, O. 2006. Control theory and fast marching techniques for brain connectivity mapping. In *Proceedings of the IEEE Computer Society Conference on Computer Vision and Pattern Recognition (New York, USA, June 2006)*, IEEE Computer Society Press, New York, USA, vol. 1, 1076–1083.

RUND, H. 1973. *The Hamilton-Jacobi Theory in the Calculus of Variations*. Robert E. Krieger Publishing Company, Huntington, N.Y.

STEJSKAL, E. O., AND TANNER, J. E. 1965. Spin diffusion measurements: Spin echoes in the presence of a time-dependent field gradient. *Journal of Computational Physics 42*, 288–292.

TIKHONOV, A., AND ARSENINN, V. Y. 1977. *Solution of Ill-Posed Problems*. John Wiley & Sons, New York.

TUCH, D. S. 2004. Q-ball imaging. *Magnetic Resonance in Medicine 52*, 1358–1372.

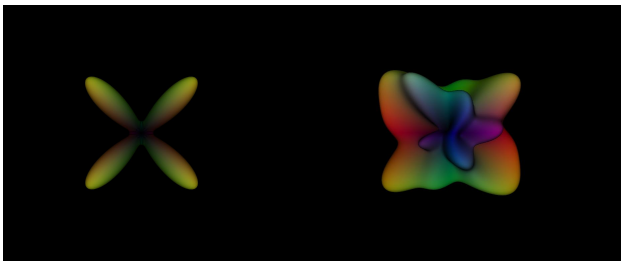

Figure 1: Left: Synthetic noise-free profile induced by two crossing fibers at right angle. Right: Same, but with Rician noise.

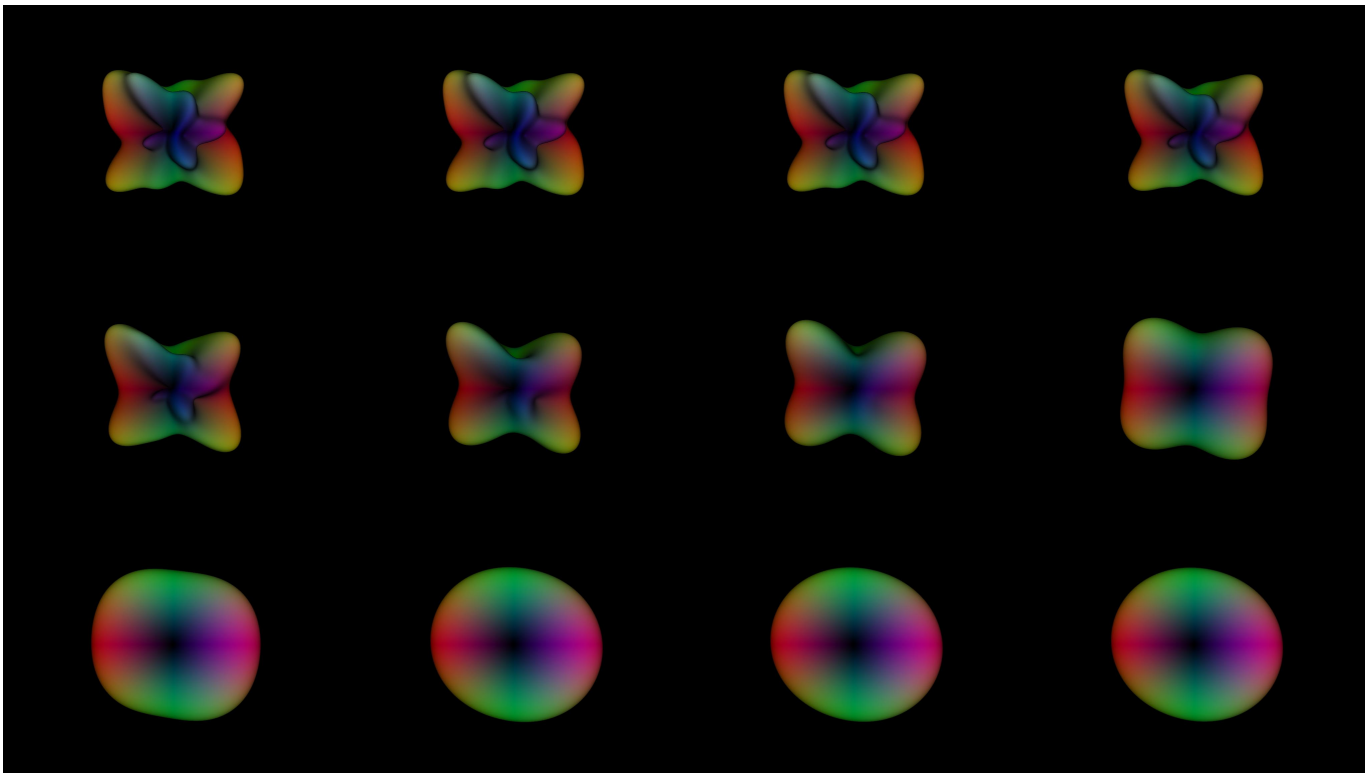

Figure 2: Regularized profiles produced from the right image in Fig. 1 using Theorem 2 for $N = 8$. The regularization parameter t increases exponentially from top left to bottom right over the range 0.007–1.0.